

# Chapter 1

## 1 Experimental Setup

The data used in this analysis were produced in  $e^+e^-$  collisions at the KEKB accelerator and collected with the Belle detector. The experiment was hosted at the High Energy Accelerator Research Organization (KEK) in Tsukuba, Japan. The experiment ran from years 1999 to 2010, collecting data at and near the energy of the  $\Upsilon(4S)$  resonance. This chapter briefly describes the accelerator and the detector, based on detailed reports from [1] and [2], respectively.

### 1.1 KEKB Accelerator

KEKB is an asymmetric  $e^+e^-$  collider, composed roughly of an electron source and a positron target, a linear accelerator (Linac) and two separate main rings with a circumference of about 3 km as shown in Figure 1.1. Electrons are first produced by a thermal electron gun and accelerated in the Linac to an energy of about 8 GeV. Part of the electrons collide with a tungsten target to produce positrons, which are accelerated in the Linac to an energy of about 3.5 GeV. Electron and positron beams are injected into the high- (HER) and low energy ring (LER) where they collide as bunches of particles at a single interaction point (IP) at an angle of about 22 mrad. The combined centre-of-mass (CM) energy of the collision corresponds to the mass of the  $\Upsilon(4S)$  resonance

$$E_{CM} = 2\sqrt{E_{e^+}E_{e^-}} = m_{\Upsilon(4S)}c^2 \approx 10.58 \text{ GeV}. \quad (1.1)$$

The  $\Upsilon(4S)$  state is produced only in a fraction of all collisions, but when it is produced, it predominantly decays to a pair of charged or neutral  $B$  mesons. This setup was chosen in accordance with the main goal of the experiment, which was to study CP violation in the  $B$  meson system. In other cases the processes include  $e^+e^-$  scattering, also known as Bhabha scattering, two-photon events, muon or tau lepton pair production, and production of  $q\bar{q}$ , where  $q = u, d, s$  or  $c$ . Table 1.1 shows the cross-sections for all mentioned interactions in collisions of  $e^+e^-$ . In addition to the nominal CM energy, the experiment collected data also at energies corresponding to other  $\Upsilon(nS)$  resonances, where  $n = 1, 2, 3, 5$ , and also at energies below the resonances.

Interaction	Cross-section [nb]
$\Upsilon(4S) \rightarrow B\bar{B}$	1.2
$q\bar{q}, q \in [u, d, s, c]$	2.8
$\mu^+\mu^-, \tau^+\tau^-$	1.6
Bhabha scattering (within detector acceptance)	44
Other QED processes (within detector acceptance)	$\sim 17$
Total	$\sim 67$

Table 1.1: Cross-sections with  $L = 10^{34} \text{ cm}^{-2}\text{s}^{-1}$  for various physics processes at  $\Upsilon(4S)$  resonance energy [2].

KEKB achieved the world-record for the peak luminosity of  $2.11 \times 10^{34} \text{ cm}^{-2}\text{s}^{-1}$ , twice as much as the designed prediction, and the total integrated luminosity of  $1041 \text{ fb}^{-1}$ . Of the full Belle dataset, about  $711 \text{ fb}^{-1}$  of data were taken at the  $\Upsilon(4S)$  energy of 10.58 GeV, which corresponds to about  $771 \times 10^6 B\bar{B}$  meson pairs.

## 1.2 Belle Detector

The Belle detector is a magnetic mass spectrometer which covers a large solid angle. It is designed to detect remnants of  $e^+e^-$  collisions. The detector is configured around a 1.5 T superconducting solenoid and iron structure surrounding the interaction point (IP). The 4-momentum of the decaying  $B$  mesons and its decayed daughter particles are determined via a series of sub-detector systems, which are installed in an onion-like shape. Short-lived particle decay vertices are measured by the silicon vertex detector (SVD) situated outside of a cylindrical beryllium beam pipe. Long-lived charged particle momentum is measured via tracking, which is performed by a wire drift chamber (CDC). Particle identification is provided by energy-loss measurements in CDC, aerogel Cherenkov counters (ACC) and time-of-flight counters (TOF), situated radially outside of CDC. Particles producing electromagnetic showers deposit energy in an array of CsI(Tl) crystals, known as the electromagnetic calorimeter (ECL), which is located inside the solenoid coil. Muons and  $K_L$  mesons (KLM) are identified by arrays of resistive plate counters in the iron yoke on the outside of the coil.

The coordinate system of the Belle detector originates at the IP, with the  $z$  axis pointing in the opposite direction of the positron beam, the  $x$  axis pointing horizontally out of the ring, and the  $y$  axis being perpendicular to the aforementioned axes. The electron beam crosses the positron beam at an angle of about  $22^\circ$ . The polar angle  $\theta$  covers the region between  $17^\circ \leq \theta \leq 150^\circ$ , while the cylindrical angle  $\varphi$  covers the full  $360^\circ$  range, amounting to about 92% coverage of the full solid angle.

### 1.2.1 Silicon Vertex Detector

SVD is the inner-most part of the Belle detector and serves the purpose of measuring the decay vertices of decaying particles. The precision of the subsystem is about  $100\ \mu\text{m}$ , which is important for measuring the difference in  $z$ -vertex positions of the  $B$  mesons in time-dependent CP violation studies. The main part of the SVD are the double-sided silicon detectors (DSSD). With their thin profile and parallel silicon strips on both sides they provide 2D hit information of charged particle and are perfect for a small-scale device which acts with high precision.

During the data taking period, two configurations were of the SVD have been used. The first, SVD1, has three layers of DSSD detectors, positioned at 30, 45.5 and 60 mm away from the IP. They compose a ladder-like structure, covering the polar angle of  $23^\circ < \theta < 140^\circ$ . This configuration was used from the beginning of the experiment until 2003, when a dataset of about  $1.52 \times 10^8$  pairs of  $B\bar{B}$  mesons were recorded. Due to problems with radiation hardness, a new configuration was used, SVD2, which was operational until the end of data taking, measuring about  $6.20 \times 10^8$  pairs of  $B\bar{B}$  mesons. The SVD2 has 4 layers of DSSD detectors positioned at 20, 43.5, 70 and 80 mm away from the IP and covered the polar angle of  $17^\circ < \theta < 150^\circ$ . The first layer was moved closer to the IP, which greatly improved the sub-system precision, due to multiple-Coulomb scattering affecting resolution more as the distance from the IP increases. The front and side view of the SVD2 are shown in Figure 1.2.

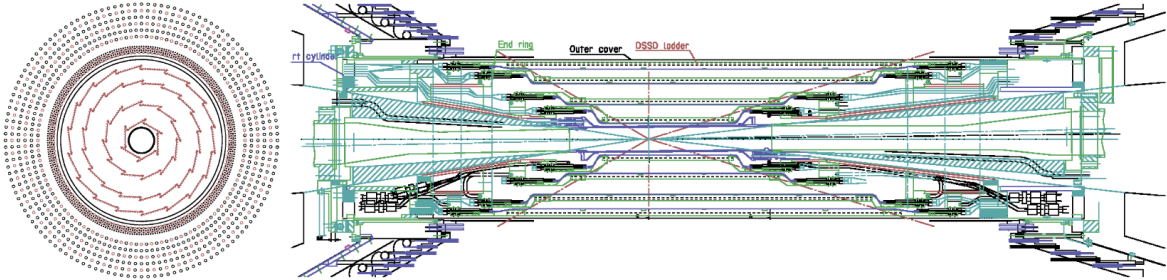


Figure 1.2: Front (left) and side (right) view of the SVD detector with the SVD2 configuration. The front view also shows the inner wires of the Drift Chamber [3].

The efficiency of the SVD was determined as a fraction of CDC tracks within the SVD acceptance that have associated SVD hits, needed for the  $B$  meson reconstruction. The average efficiency is found to be around 98% and is in agreement with simulation. SVD performance is also determined via the impact parameter  $z$  and  $r\phi$  resolution, which was obtained from cosmic ray data. The momentum and angular dependence of the impact parameters is shown in Figure 1.3 and is well represented by the following parametriza-

tion for the SVD2

$$\sigma_z = 28 \mu\text{m} \oplus \frac{32 \mu\text{m}}{(p/(1 \text{ GeV}/c)) \beta \sin^{5/2} \theta}, \quad (1.2)$$

$$\sigma_{r\phi} = 22 \mu\text{m} \oplus \frac{36 \mu\text{m}}{(p/(1 \text{ GeV}/c)) \beta \sin^{3/2} \theta}, \quad (1.3)$$

where  $p$  is the particle momentum,  $\theta$  is the polar angle, and  $\beta = v/c$ . An advantage of the smaller distance between the IP and the first DSSD layer in SVD2 is clearly seen.

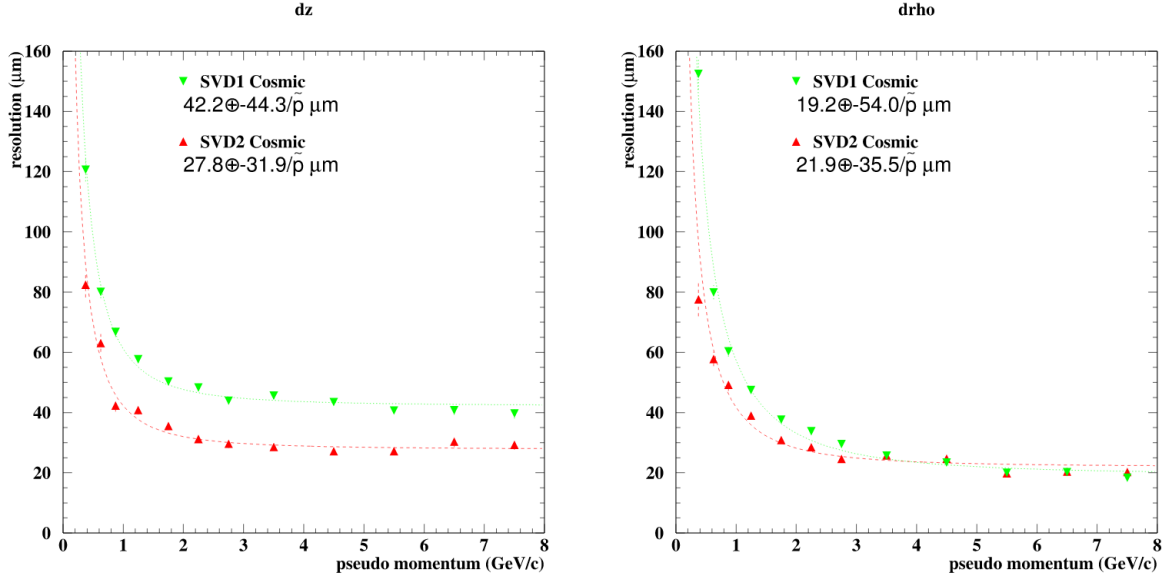


Figure 1.3: Impact parameter resolutions of  $z$  (left) and  $r\phi$  (right) coordinates for the SVD1 and SVD2 configuration of the vertex detector [3].

## 1.2.2 Central Drift Chamber

CDC is a large-volume tracking device located at the central part of the Belle detector and is crucial for measurements of the particle trajectories and momenta, but also serves as a particle identification device (PID). It has a cylindrical structure with a radius of 88 cm, length of 2.4 m and acceptance equal to the one of SVD2. The chamber has a total of 8400 wires, which are positioned in 50 layers and describe a nearly square wire configuration. There are two types of wires – field wires for producing the electrical field, and sense wires for detecting the particles. Odd-numbered wire layers are oriented in the  $z$  direction and provide measurement of the transverse momentum  $p_t$ , while even-numbered wires are inclined with respect to the  $z$  axis by a small angle of  $\pm 50$  mrad to allow for measuring of the polar angle of the track. The wire configuration is shown

in Figure 1.4. The space between the wires is filled with a gas mixture of 1 : 1 helium-ethane, a low- $Z$  gas in order to minimize multiple-Coulomb scattering contributions to momentum resolution, since the majority of particles in  $B$  events have a momentum lower than 1 GeV/ $c$ . It also has a small cross section of the photoelectric effect, which is important to reduce background electrons induced by the synchrotron radiation from the beam.

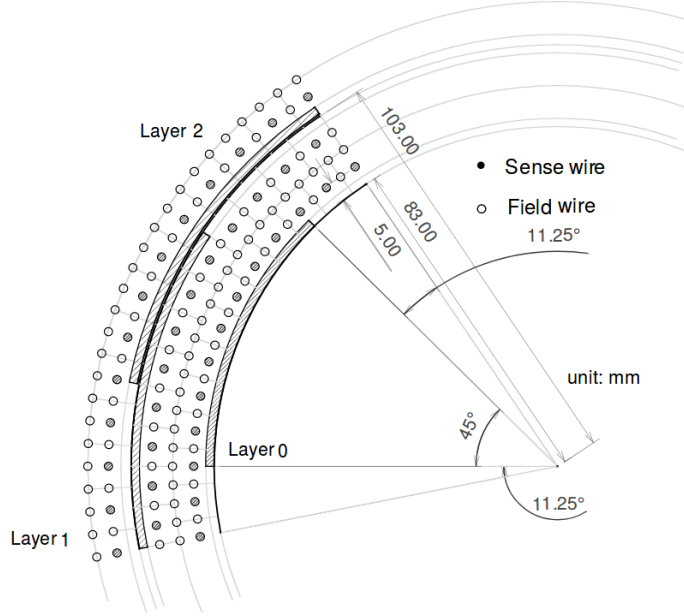


Figure 1.4: Cell structure of CDC [2].

Charged particles which pass the CDC wire frame cause gas ionization. The produced electrons drift toward the sense wires with great acceleration due to the strong electric field close to the wire. The accelerated electrons collide with gas molecules and produce secondary, tertiary etc. ionizations, which result in an electron avalanche, a process which increases the signal by many orders of magnitude. The primary electrons also have a specific drift velocity, which allows us to relate the measured pulse height and drift time to the energy deposit of the particle as well as the distance from the sense wire. This information is important for calculating the energy loss  $dE/dx$ .  $dE/dx$  as a function of momentum differs for different particles, as shown in Figure 1.5. This allows for identification purposes of, specifically for kaons and pions. In the momentum region less than 0.8 GeV/ $c$ ,  $dE/dx$  enables a separation between kaons and pions up to  $3\sigma$ . The resolution of the transverse momentum measurement with the CDC is a function of the transverse momentum itself, as well as the particle velocity, and is parametrized as

$$\sigma(p_T)/p_T = \frac{0.201\% p_T}{1 \text{ GeV}/c} \oplus \frac{0.290\%}{\beta}. \quad (1.4)$$

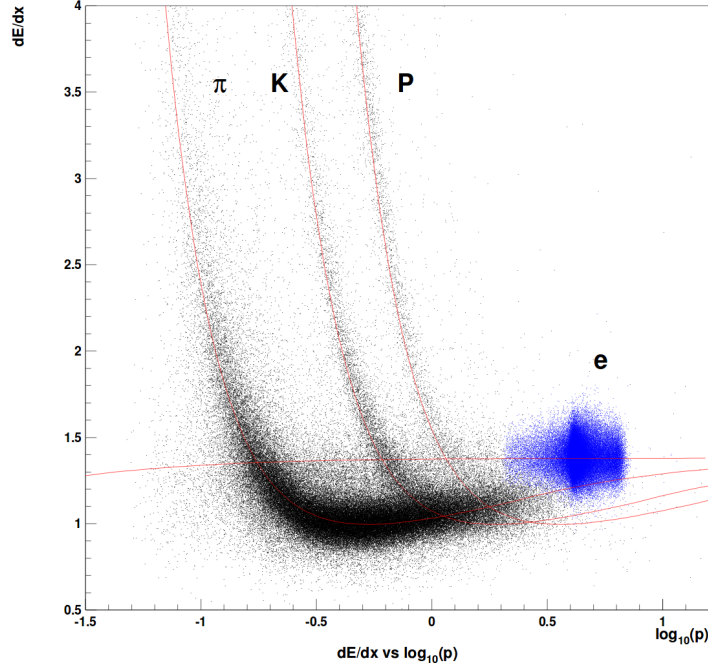


Figure 1.5: Measured  $dE/dx$  as a function of particle momentum. The red lines show the expected distribution for different types of particles [2].

### 1.2.3 Time-of-Flight Counter

The purpose of the TOF subdetector is particle identification in the momentum region  $0.8 \text{ GeV}/c < p < 1.2 \text{ GeV}/c$ , especially for kaons and pions. There are 64 TOF modules in the barrel region, covering the polar angle of  $33^\circ < \theta < 121^\circ$ . One TOF module consists of two long polyvinyltoluene-based plastic scintillator bars, 4 fine-mesh photomultiplier tubes (PMT) at the 4 ends of the bars, and a trigger scintillation counter, where the latter provides additional trigger information. TOF measures the time interval between the  $e^+e^-$  collision and the passage of the particle through it. The mass of a particle can be inferred via the relation

$$m^2 = \left( \frac{1}{\beta^2} - 1 \right) p^2 = \left( \frac{T^2 c^2}{L^2} - 1 \right) p^2, \quad (1.5)$$

where  $T$  is the measured time interval,  $L$  is the charged particle trajectory length from the IP to TOF and  $p$  is the charged particle momentum, determined by SVD and CDC. The resulting mass distribution for charged tracks measured by TOF in hadron events is shown in Figure 1.6, where clear peaks corresponding to pions, kaons and protons can be seen. To achieve the good discrimination between kaons and pions, a time-of-flight resolution of less than 100 ps is needed for particles with momentum below about

1.2 GeV/c, which encompasses 90% of the particles produced in  $\Upsilon(4S)$  decays. The identification power can also be determined in the form of  $\pi^\pm/K^\pm$  separation significance as a function of particle momentum, shown in Figure 1.7. A clear separation of about  $2\sigma$  is achieved for particle momenta up to 1.25 GeV/c.

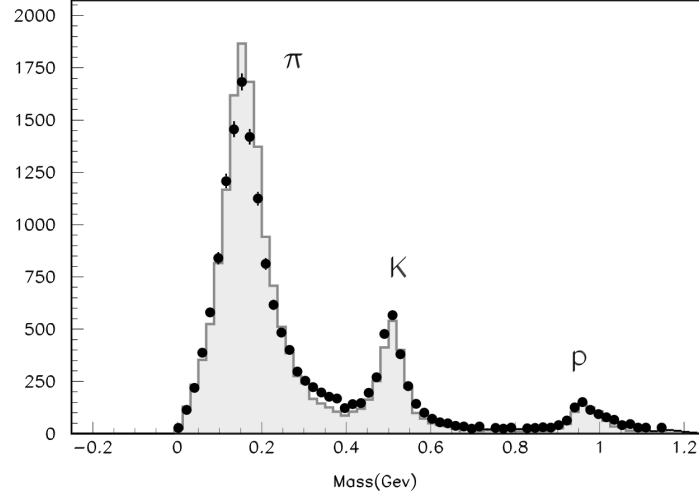


Figure 1.6: Mass distribution from TOF measurements for particle momenta below 1.2 GeV/c [2].

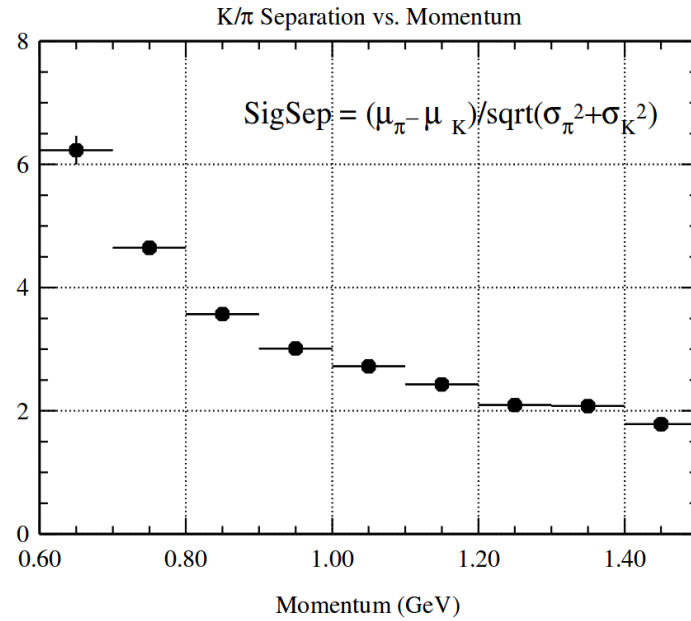


Figure 1.7:  $\pi^\pm/K^\pm$  separation by TOF [2].



### 1.2.4 Aerogel Cherenkov Counter

TOF is not capable of performing good PID above  $1.2 \text{ GeV}/c$  momentum, since  $\beta$  is almost equal to 1. For higher momenta in the region  $1.0 \text{ GeV}/c < 4.0 \text{ GeV}/c$ , the ACC is introduced. It is a threshold-type Cherenkov counter which utilizes the fact that particles emit Cherenkov light if the particle speed is greater than the speed of light in the passing medium. ACC is introduced in the barrel region with 960 separate modules, covering a polar angle of  $34^\circ < \theta < 127^\circ$  and 228 modules in the forward end-cap region, with the polar angle coverage of  $17^\circ < \theta < 34^\circ$ . Each ACC module consists of an aluminum encased block of silica aerogel and one or two fine-mesh PMTs encased on each block to detect Cherenkov light pulses. Due to the polar angle dependence of the particle momentum, 6 different refractive indices are chosen for the aerogel material, ranging from 1.010 up to 1.030 and are controlled within 3% precision. The layout of the ACC is shown in Figure 1.8.

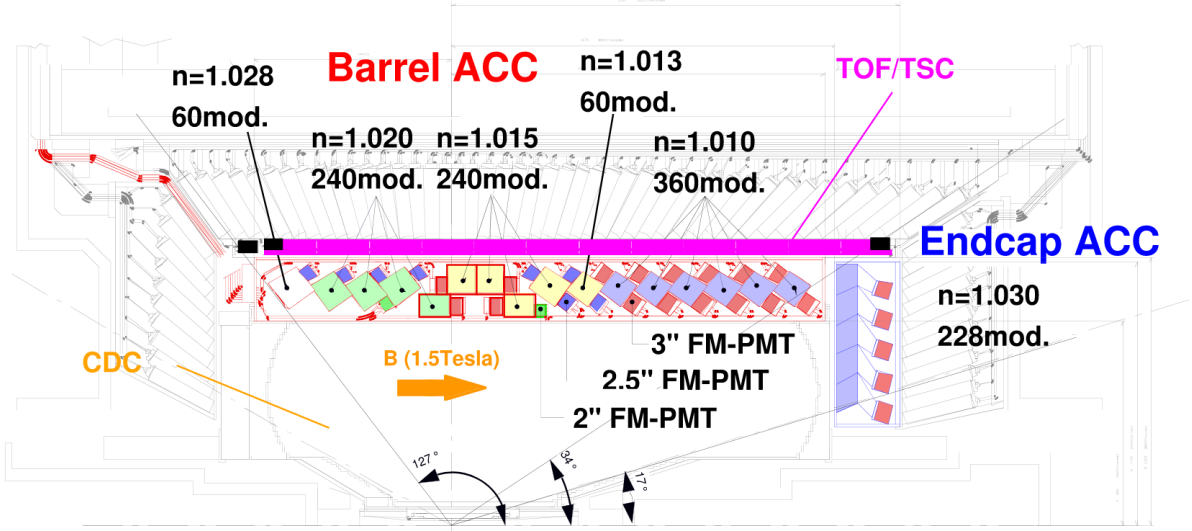


Figure 1.8: Cross-sectional view of the CDC (inner most), ACC and TOF (outer most) detectors [2].

The threshold velocity  $\beta$  of a given particle for Cherenkov radiation is

$$\beta \leq \frac{1}{n}, \quad (1.6)$$

where  $n$  is the refractive index of the medium. The refractive indices in the ACC are such that, due to different masses, pions will emit Cherenkov light and kaons will not, due to different masses of the particles. Using the PID of ACC, along with other sub-system PID info, the electron identification efficiency in the momentum range above  $1 \text{ GeV}/c$  is equal to or above 90% while the pion fake rate, the probability of wrongly

identifying pions as electrons, to be around 0.2 - 0.3%. Similarly for kaons, kaon ID efficiency is equal to 80% for most of the momentum region up to 4 GeV/c, while pion fake rate remains below 10%. Figure 1.9 shows the electron and kaon efficiencies and the corresponding pion fake rates as a function of particle momenta.

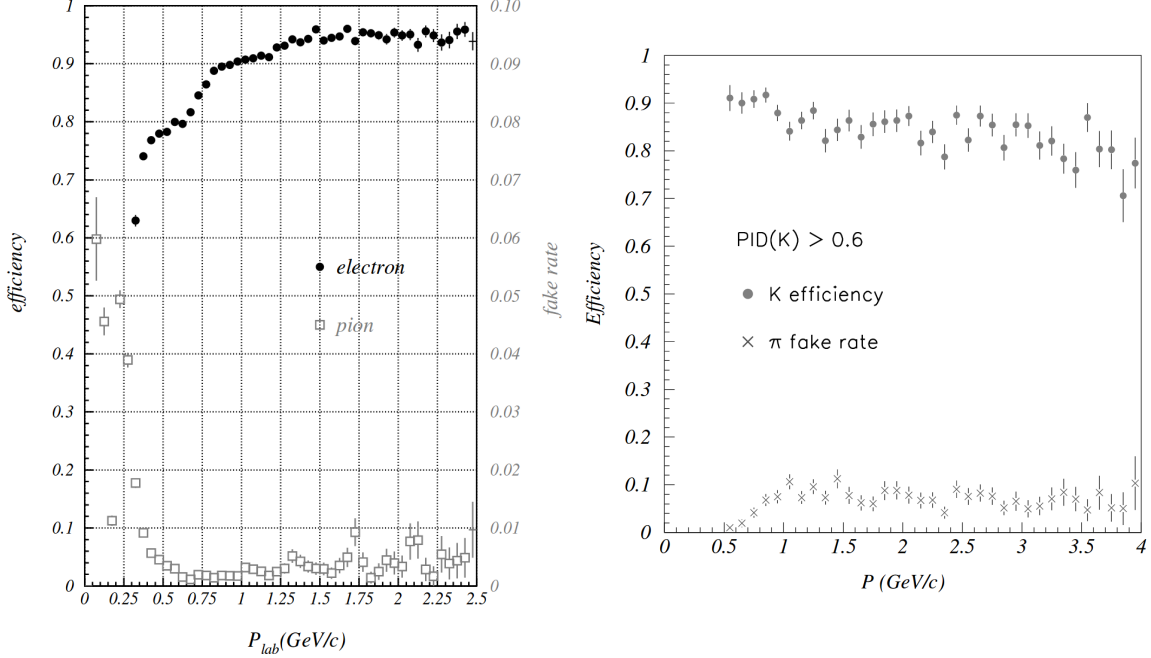


Figure 1.9: Electron identification efficiency and fake rate for charged pions (left) and similarly for kaons (right). Note the different scales for the electron efficiency and fake rate in the former case [2].

## 1.2.5 Electromagnetic Calorimeter

Measurement of position and energy deposit of particles is performed in the ECL, especially for electrons and photons, where the latter are not measured by any of the subsystems described so far. It also provides complimentary particle identifications for electrons versus pions. The calorimeter consists of a highly segmented array of thallium-doped caesium iodide (CsI(Tl)) in the form of tower-shaped crystals, each pointing towards the IP. Each crystal is about 30 cm long with a width from 44.5 mm to 65 mm in the barrel, and from 44.5 mm to 82 mm in the end-caps. Out of a total of 8736 crystals with a total mass of about 43 tons, 6624 of them are positioned in the barrel region and 1152 (960) in the forward (backward) end-caps. The inner radius of the barrel section is about 1.25 m, while the end-caps are positioned at  $-1.0$  m and  $2.0$  m from the IP in direction of the  $z$  axis. The polar angle coverage of the barrel region is  $32.2^\circ < \theta < 128.7^\circ$ , and for the end-caps  $12.4^\circ < \theta < 31.4^\circ$  and  $130.7^\circ < \theta < 155.1^\circ$ .

160 Figure 1.10 shows the layout of the barrel and end-caps ECL.

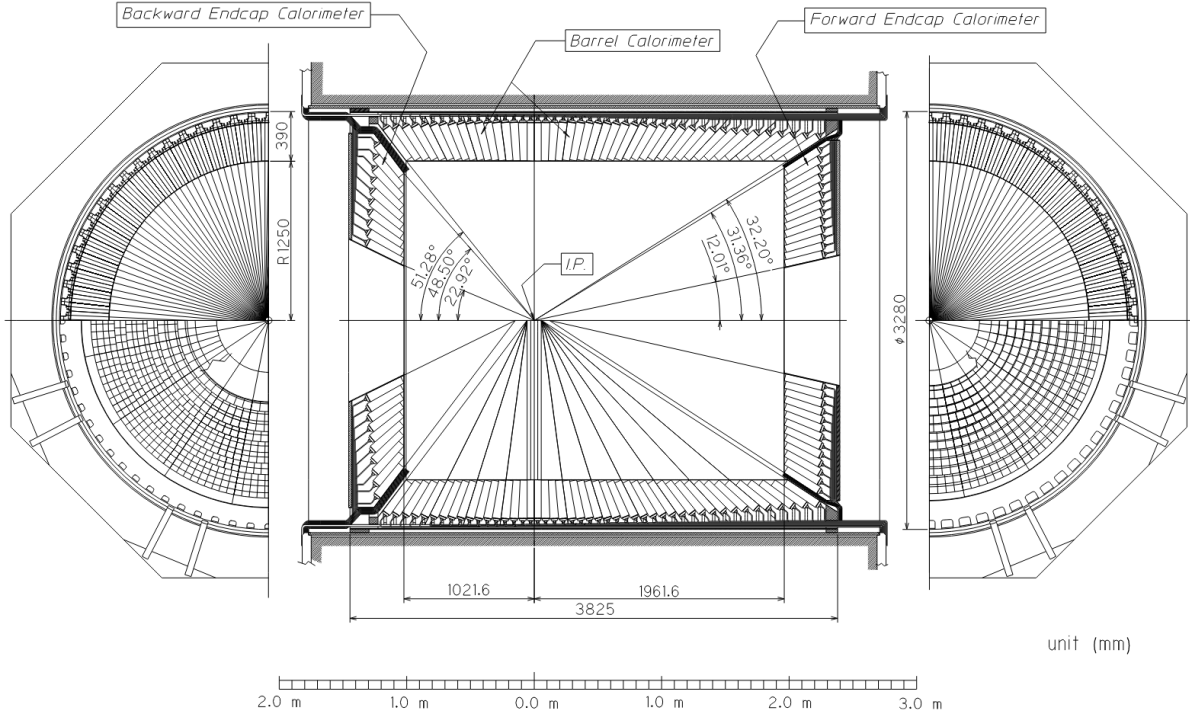


Figure 1.10: Overall configuration of the ECL [2].

161 When an electron or a photon hits a crystal, it produces an electromagnetic shower, a re-  
 162 sult of the bremsstrahlung and pair-production effects. Heavier charged particles do not  
 163 interact in the same way and deposit only a small amount of energy by ionization effects.  
 164 The information from the ECL, compared with momentum measurements provided by  
 165 the CDC, enables the identification of electrons. The distribution of the deposited en-  
 166 ergy for different particles is shown in Figure 1.11. The probability of misidentifying an  
 167 electron as a pion is approximately 5% for momenta less than 1 GeV/ $c$ , and less than  
 168 1% for momenta above 2 GeV/ $c$ .

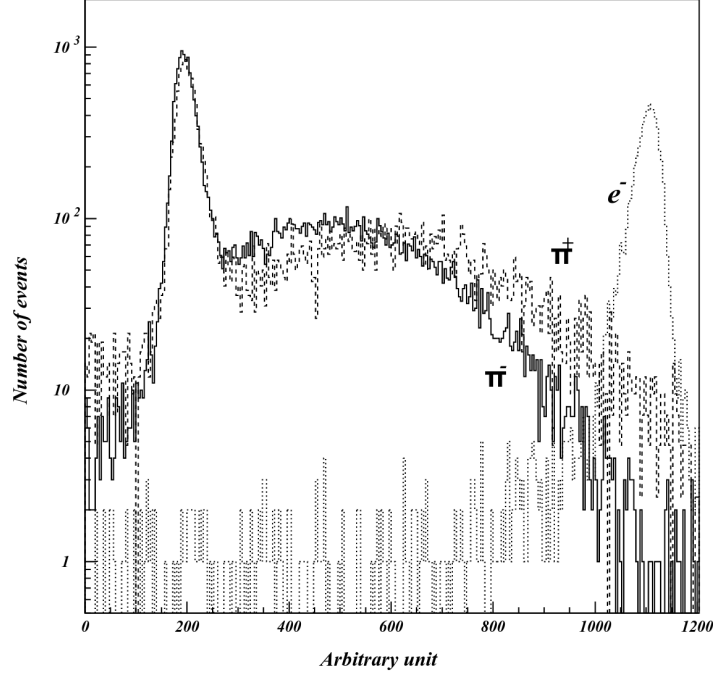


Figure 1.11: Distribution of the energy deposit by electrons and charged pions at 1 GeV/ $c$  momentum [2].

169 For ECL calibration,  $e^+e^- \rightarrow e^+e^-$  and  $e^+e^- \rightarrow \gamma\gamma$  events were used. The average  
 170 energy resolution was achieved to be 1.7% for the barrel ECL, and 1.74% and 2.85% for  
 171 the forward and backward ECL, respectively, as shown in Figure 1.12. These value are  
 172 in good agreement with Monte Carlo predictions. Worse energy resolution in backward  
 173 end-cap is due to the lower photon energy, which results in larger effects of passive  
 174 material in front of the calorimeter [3]. The energy resolution as a function of energy  
 175 can be obtained via the following relation

$$\frac{\sigma_E}{E} = \frac{0.0066\%}{(E/1 \text{ GeV})} \oplus \frac{1.53\%}{(E/1 \text{ GeV})^{1/4}} \oplus 1.18\%, \quad (1.7)$$

176 while the resolution of the position measurement is

$$\sigma_{pos} = 0.27 \text{ mm} + \frac{3.4 \text{ mm}}{(E/1 \text{ GeV})^{1/2}} + \frac{1.8 \text{ mm}}{(E/1 \text{ GeV})^{1/4}}. \quad (1.8)$$

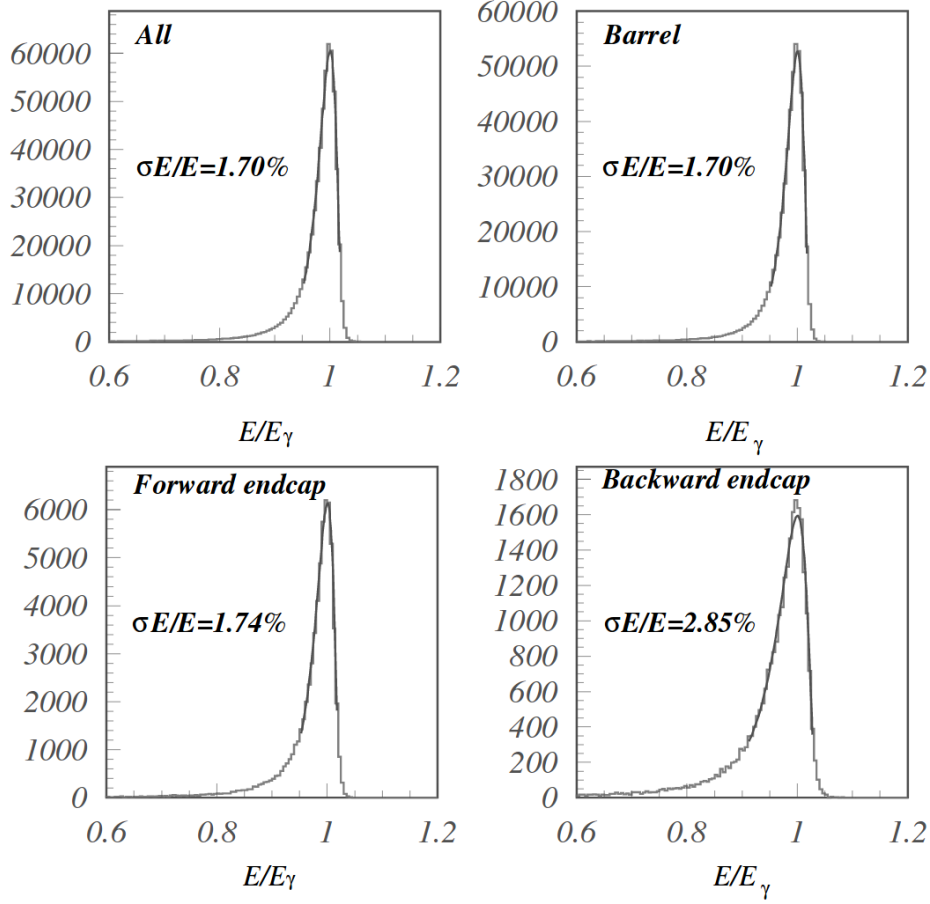


Figure 1.12: Reconstructed energy distribution for  $e^+e^- \rightarrow \gamma\gamma$  events for overall, barrel, forward and backward end-cap calorimeters [2].

### 1.2.6 $K_L^0/\mu$ Detector

The KLM detector is used for detection of high-penetration particles such as  $K_L^0$  and  $\mu$  for momenta larger than 0.6 GeV/c. The setup covers the polar angle of  $20^\circ < \theta < 155^\circ$ . Detection of  $K_L^0$  particles is troublesome, since they are neutral and have a small material interaction probability, therefore a lot of material is needed in the KLM. To provide detection of both kinds of particles, hadronic and neutral, as well as electromagnetically and hadronically interacting, the KLM is constructed as a sampling calorimeter, which consists of 15 layers of 3.7 cm thick resistive-plate counters (RPC) with 14 layers of 4.7 cm thick iron plates between them. A single RPC module consists of two parallel plate electrodes, two glass panels, and gas in between. A charged particle passing the gas gap initiates a local discharge of the plates, which in turn induces signal to record the time and location of ionization. This is possible since the resistivity of the glass surface

is high, so the discharge occurs locally. Hadrons interacting with the iron plates may produce a shower of ionizing particles, which are then also detected by the RPCs. The KLM is located outside of superconducting solenoid and the iron plates of the KLM serve a dual role as the flux return for the magnetic field. Figure 1.13 shows a cross-section of an RPC superlayer, consisting of an RPC pair.

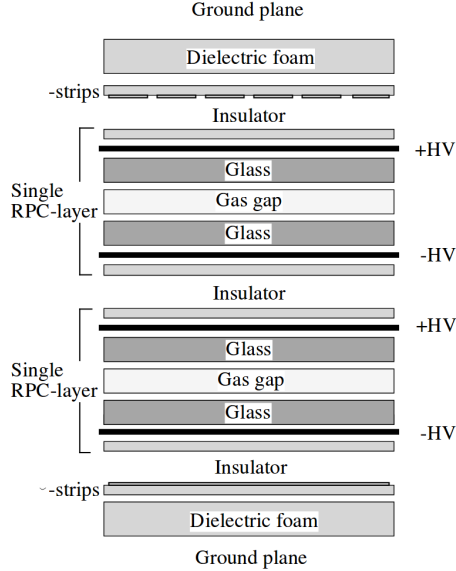


Figure 1.13: Cross-section of an RPC superlayer, consisting of an RPC pair [2].

The  $K_L^0$  particle can be distinguished from other charged hadrons because they have no matched track in the CDC. The flight direction can also be inferred from the hit locations in the consecutive RPCs. Tracks of charged particles measured in CDC are extrapolated into KLM and clusters within  $15^\circ$  of an extrapolated charged particle track are excluded from  $K_L^0$  cluster candidates. On the other hand, muons with matched CDC tracks are able to reach the KLM if their momentum is larger than  $0.5 \text{ GeV}/c$ . They do not interact strongly and do not produce hadronic showers in the KLM, which serves as a handle on the muon identification. Figure 1.14 (left) shows the number of neutral clusters per event and a Monte Carlo simulation of the predicted number of  $K_L^0$  clusters per event. The average number of  $K_L^0$  clusters per event is 0.5. The agreement with the prediction gives us the confidence that the detector and our reconstruction software are performing correctly. Figure 1.14 (right) shows the muon detection efficiency as a function of momentum and shown for a likelihood cut of 0.66, where muon likelihood is based on the comparison of the measured range of a particle with the predicted range for a muon. Based on  $K_S \rightarrow \pi^+\pi^-$  events, a muon identification efficiency of better than 90% is determined, with a pion fake rate of less than 5% for particles with momenta more than  $1.5 \text{ GeV}/c$  and a likelihood cut of 0.66.

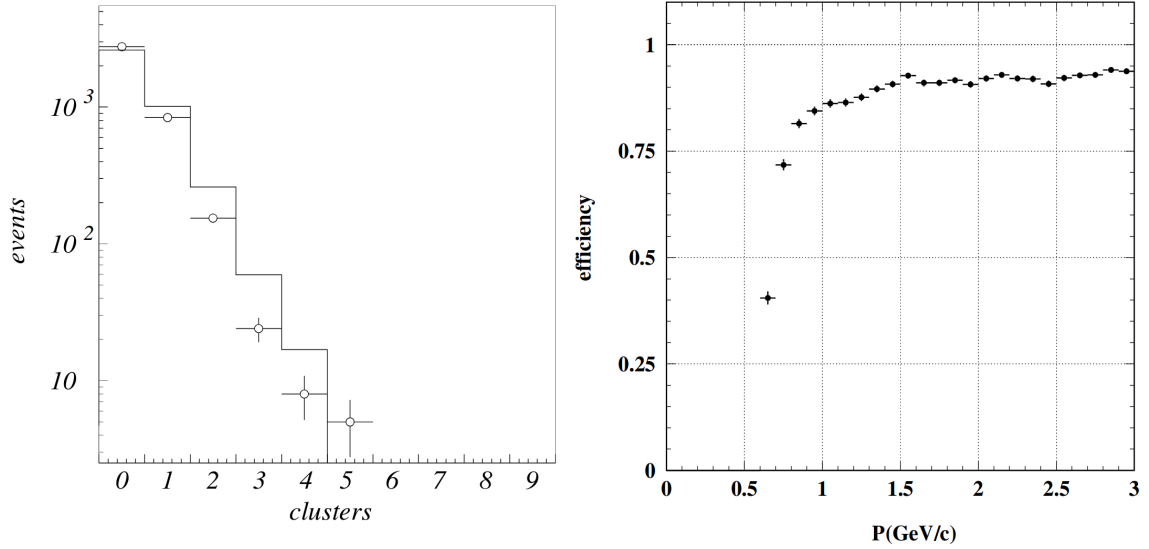


Figure 1.14: Number of neutral clusters per event in KLM (left) and muon detection efficiency as a function of momentum in KLM (right) [2].

211 Cosmic ray events have been used to determine efficiency and resolution of the KLM,  
 212 with an overall efficiency typically over 98%. The temporal and spatial resolution of the  
 213 KLM are few ns and about 1.2 cm, respectively. The latter corresponds to an angular  
 214 resolution from the interaction point of better than 10 mrad.

### 215 1.3 Trigger, Data Acquisition and Computing 216 Systems at Belle

217 In order to to detector calibration and proper luminosity measurements, we need to  
 218 accumulate samples of Bhabha and  $\gamma\gamma$  scattering. Otherwise, as shown in Table 1.1, the  
 219 cross-section for physics events of interest is reasonably small. During normal operation  
 220 (luminosity of  $L = 10 \times 10^{34} \text{ cm}^{-2}\text{s}^{-1}$ ) the total event rate is around 200 Hz. Out  
 221 of this rate, 100 Hz are physically interesting events, which include also two photon  
 222 events, Bhabha scattering and  $\mu$  pair production, besides hadronic events from  $B\bar{B}$  pair  
 223 events. In order to discard events which are not interesting for physics analyses, we use  
 224 a trigger system by appropriately applying restrictive conditions. This section describes  
 225 the necessary procedures and equipment to successfully do so.

### 1.3.1 Trigger System

The trigger system operates by immediately eliminating events that are not of interest, so that the amount of stored data is within the 500 Hz frequency limit of the data acquisition system (DAQ) [2], while the efficiency for physics events of interest is kept high. Events which pass the triggers are then stored, otherwise discarded. The Belle trigger system consists of three stages, Level-1, Level-3 and Level-4.

Level-1 trigger is the first stage of the trigger system, which consists of multiple sub-detector triggers, all connected to a central trigger system called the Global Decision Logic (GDL). Each sub-detector trigger works on a principle of either a track trigger or an energy trigger. In the former case the triggers discard events not meeting conditions based on the number of reconstructed tracks or track hits, while the latter is based on the total energy deposit and counting of crystal hits. Each sub-detector processes the event information and provides it to the GDL, where all the information is combined and the current event is characterized. The information from the sub-detector triggers reaches the GDL within  $1.85 \mu\text{s}$  after the collision, and the final trigger signal is provided within at a fixed  $2.2 \mu\text{s}$  latency. The combined efficiency from the Level-1 trigger is greater than 99.5% for hadronic events.

### 1.3.2 Data Acquisition Sytem

### 1.3.3 Computing System



## Bibliography

- [1] T. Abe et al. “Achievements of KEKB”. In: *Progress of Theoretical and Experimental Physics* 2013.3 (2013), 03A001. DOI: [10.1093/ptep/pts102](https://doi.org/10.1093/ptep/pts102). eprint: [/oup/backfile/content\\_public/journal/ptep/2013/3/10.1093/ptep/pts102/2/pts102.pdf](http://backfile/content_public/journal/ptep/2013/3/10.1093/ptep/pts102/2/pts102.pdf). URL: <http://dx.doi.org/10.1093/ptep/pts102>.
- [2] A. Abashian et al. “The Belle detector”. In: *Nuclear Instruments and Methods in Physics Research Section A: Accelerators, Spectrometers, Detectors and Associated Equipment* 479.1 (2002). Detectors for Asymmetric B-factories, pp. 117–232. ISSN: 0168-9002. DOI: [https://doi.org/10.1016/S0168-9002\(01\)02013-7](https://doi.org/10.1016/S0168-9002(01)02013-7). URL: <http://www.sciencedirect.com/science/article/pii/S0168900201020137>.
- [3] J Haba. “Letter of Intent for KEK Super B Factory, Part II: Detector”. In: *KEK Report* (2004), pp. 04–4. URL: [http://superb.kek.jp/documents/loi/img/LoI\\_detector.pdf](http://superb.kek.jp/documents/loi/img/LoI_detector.pdf).